

# Matrix Multiplication-Driven Repulsive Fields for 3D Voxel-Based TSDF Calculation

Jakob Baumgartner<sup>1</sup> and Gregor Klančar<sup>2</sup>

*Abstract—*

## I. INTRODUCTION

In dynamic environments, a robot manipulator must swiftly respond to emerging obstacles. Our approach enables the robot to determine safe movement directions and velocities by real-time assessment of nearby space for obstacles.

In 3D graphics, a voxel is like a tiny cube in a grid that makes up the 3D space. We use voxels to represent the workspace of the robot, each voxel has a value that tells us if it's probabilistically empty or occupied. A zero means empty, and a one means definitely something is there, with values in between showing varying levels of certainty.

The occupancy grid of voxels can be set in advance to match the layout of the space. We can also change the values in the voxels if we know where other objects or agents are moving. Besides pre-setting, we can use depth sensors to detect what's around.

Our method calculates repulsive velocities from existing occupancy voxel grid, which are vectors that guide the robot on where to go by pointing away from potential collisions. These vectors gain strength as the robot approaches an obstacle, signaling an urgent need to maneuver to safety. Conversely, when the robot is positioned at an equal distance from obstacles in the vicinity—safely away from all potential collisions—the repulsive velocities weaken because there's no immediate need to move.

Repulsive velocities tell the agent in which direction to move, so that it avoids nearby obstacles. These velocities drop to zero when the agent maintains a minimum safe distance from obstacles, and rise to their highest when it nears an obstacle, facilitating immediate evasive action. As the repulsive field calculation is locally based, it will also go to zero when the agent is surrounded by all directions, equally spaced from all sides. That is, it is in the best local minima away from all the obstacles in its proximity.

## II. RELATED WORKS

ADD

## III. REPULSIVE FIELD CALCULATION

This section introduces our novel approach for calculating repulsive fields, a critical component in enabling robots to detect and avoid obstacles in real-time. By leveraging a voxel-based representation of the surrounding space, our method dynamically assesses potential collision threats and calculates directional repulsive velocities. These velocities are essential for guiding the robot away from obstacles,

ensuring smooth and safe navigation through complex environments. Our innovative use of kernel convolution methods allows for the precise calculation of avoidance velocities, providing a robust solution for obstacle avoidance that can be integrated seamlessly into robotic control systems. The following subsections delve into the technical details of our approach, including the mapping of Cartesian space to a discrete occupancy grid, kernel selection for optimized field calculation, and the application of tri-linear interpolation for smooth velocity transitions.

### A. KERNELS AND THEIR MATRIX APPLICATIONS

The fundamental concept of our directional kernels lies in computing the repulsive field individually for each direction within the Cartesian coordinate system.

Our kernels are designed as three-dimensional matrixes with a primary kernel axis aligned along a specific Cartesian direction, corresponding to the calculated repulsive velocity. The two secondary kernel axes are orthogonal to this primary axis. The distribution of values along the primary axis is inversely symmetric, exhibiting positive values on one side and negative values on the other, with the zero valued cell in the center of the kernel, where jump between max positive and max negative magnitude is. The function of the increase in magnitude along the primary axis of the kernel defines the shape of the repulsive velocity field, determining how the repulsive velocity changes as the agent approaches an obstacle. Moreover, it is essential for the magnitudes at the kernel's periphery to be minimal, promoting a smooth increase in repulsive velocity when approaching the obstacle rather than a sudden spike.

We introduce two distinct distributions for the primary axis weights, although other distributions could also be applicable. The selection of weight distribution is contingent on the desired profile of repulsive velocities within the Artificial Potential Field (APF).

The inaugural proposed function adheres to a mirrored normal or Gaussian distribution, wherein adjusting the standard deviation ( $\sigma$ ) modulates the rate at which field values escalate as obstacles are approached.

The terms  $\Delta i = c_i - i$ ,  $\Delta j = c_j - j$ , and  $\Delta k = c_k - k$  denote the displacement count from the matrix's central field, where the field components are calculated, in their respective coordinate directions.

$$w_{\Delta i} = \begin{cases} e^{-\frac{\Delta i^2}{2\sigma^2}} / (\sigma\sqrt{2\pi}) & \text{if } \Delta i > 0 \\ 0 & \text{if } \Delta i = 0 \\ -e^{-\frac{\Delta i^2}{2\sigma^2}} / (\sigma\sqrt{2\pi}) & \text{if } \Delta i < 0 \end{cases} \quad (1)$$

Another distribution we used is mirrored linear, where the  $\Delta i_{max} = \lfloor \frac{\text{range}}{\Delta R} \rfloor$  is the rounded down half length of the primary axis kernel.

$$w_{\Delta i} = \begin{cases} \frac{\Delta i_{max} - \Delta i}{\Delta i_{max}} & \text{if } \Delta i > 0 \\ 0 & \text{if } \Delta i = 0 \\ \frac{\Delta i_{max} + \Delta i}{\Delta i_{max}} & \text{if } \Delta i < 0 \end{cases} \quad (2)$$

The length  $i_{max}$  of the primary axis is critical, as it dictates the detection range for obstacles. Longer kernels can detect obstacles further away from the robot, essentially extending the 'safety zone' around the robot. If the primary axis is too long, it can lead to extra calculations and may cause the robot to unnecessarily avoid obstacles that aren't in its immediate path, making its movement and path planning less efficient.

If the matrix would be only 1 field width and height the field would work kind of as ray tracing in each of the main cartesian coordinate directions. Since our need is to detect also obstacles that don't align perfectly along the cartesian direction, it is important that our matrixes have width and height. However as we want bigger repulsive field when the obstacle is head on in the direction than when the obstacle is off the cardinal direction, we propose the following multiplier, to account for the off direction obstacles.

The length  $\Delta j_{max} = \lfloor \frac{\text{width}}{2\Delta R} \rfloor$  of the orthogonal axes influences the peripheral detection range for obstacles. Excessively wide kernels may generate repulsive velocities for objects that are not in the path of the robot, whereas too narrow kernels might only detect obstacles aligned directly with the Cartesian direction in the point of interest. When selecting the width and height of the kernel, we must consider the density of the neighboring points of interest on the agent, ensuring that the combination of kernels adequately cover the entire agent's surrounding area.

For point-based agents, such as quadcopters, it is practical to align the dimensions of each matrix—length, width, and height—to be identical. This configuration ensures uniform coverage of the spherical area surrounding the agent and reduces the risk of blind spots that might occur when obstacles are close to the agent but situated between the discrete kernels.

For smooth transitions when approaching the obstacles we propose the following sinus based function for the orthogonal axis distributions. The proposed equation is the same for both of the orthogonal matrix axis.

$$w_{\Delta j} = \begin{cases} \sin(|\Delta j| \pi / (2\Delta j_{max})) & \text{if } \Delta j < 0 \text{ or } \Delta j > 0 \\ 1 & \text{if } \Delta j = 0 \end{cases} \quad (3)$$

Another option is to use linearly falling weights.

$$w_{\Delta j} = \begin{cases} \frac{\Delta j_{max} - \Delta j}{\Delta j_{max}} & \text{if } \Delta j < 0 \text{ or } \Delta j > 0 \\ 1 & \text{if } \Delta j = 0 \end{cases} \quad (4)$$

Finally we get three matrix kernels, one for each of the three coordinate axis directions by multiplying weights components for primary and orthogonal axis.

$$w_{\Delta i \Delta j \Delta k} = w_{\Delta i} * w_{\Delta j} * w_{\Delta k} \quad (5)$$

Following the establishment of repulsive kernel weights, kernel multiplication is employed to ascertain the repulsive velocity components within Cartesian space. We select a corresponding segment from the obstacle grid, aligning in size and centered around the point of interest (POI) on the robot, where we want to calculate the repulsive velocities. This results in two identically sized 3D matrices: one serving as a "window" into the obstacle grid ( $A_d$ ) and the other as the representative kernel ( $K_d$ ).

Positioning of the agent at the edge of the known voxel grid necessitates a strategic decision regarding the window's boundary elements. These elements, located beyond the matrix's spatial domain, can either be considered vacant—encouraging the robot to explore these new areas—or occupied—thereby deterring the robot from exiting the mapped grid space.

Applying the Hadamard (element-wise) product to the segment of the obstacle grid  $G_d$  and the kernel  $W_d$  results in a new matrix for each Cartesian direction ( $d \in \{x, y, z\}$ ). By summing over all values in this resultant matrix, we calculate the repulsive velocity component for that specific direction. This process is independently conducted for each Cartesian coordinate, ultimately yielding the comprehensive repulsive velocity vector  $\vec{v}_i = [v_{x_i}, v_{y_i}, v_{z_i}]$ .

$$v_d = \sum_{i,j,k} (G \odot W)_{ijk} = \sum_i \sum_j \sum_k g_{\Delta i \Delta j \Delta k} w_{\Delta i \Delta j \Delta k} \quad (6)$$

PLOT: kernel 2D images

### B. 3D INTERPOLATION

The occupancy grid's representation of the robot's environment is inherently discrete, possessing finite resolution, in contrast to the continuous nature of Cartesian space. The approximation or rounding necessary to transition from Cartesian coordinates to discrete grid representations may introduce discontinuities in the calculated repulsive field. To counteract this, tri-linear interpolation is utilized, facilitating a smooth transition to a continuous repulsive field value, as illustrated in Fig. 1.

Maintaining a smooth change in velocity contributions to the robot is crucial. However, the discrete nature of our obstacle grid presents a challenge in achieving complete continuity. While enhancing the obstacle grid's resolution could theoretically yield a more continuous behavior, practical limitations arise due to the finite resolution of sensors and the grid representation itself. Moreover, an increase in

resolution would inevitably require more memory for storing the occupancy grid and additional computational resources. Thus, to ensure velocity continuity across adjacent cells within the obstacle grid for a point of interest (POI), trilinear interpolation is employed.

We start by scaling the coordinates of POI into the grid coordinate system, by multiplying it by grid resolution (eq. 7).

$$\vec{P} = \vec{p}_{\text{POI}} \times \Delta R \quad (7)$$

We get the indexes of the surrounding cells by first scaling the POI position by grid resolution and then rounding the position to the nearest lower and upper integer positions (eq. 8).

$$\vec{P} = \begin{bmatrix} X \\ Y \\ Z \end{bmatrix} = \begin{bmatrix} \lfloor \vec{p}_{\text{POI}}(1) \rfloor & \lceil \vec{p}_{\text{POI}}(1) \rceil \\ \lfloor \vec{p}_{\text{POI}}(2) \rfloor & \lceil \vec{p}_{\text{POI}}(2) \rceil \\ \lfloor \vec{p}_{\text{POI}}(3) \rfloor & \lceil \vec{p}_{\text{POI}}(3) \rceil \end{bmatrix} \quad (8)$$

Once we got the indexes of the eight surrounding cells of our POI, we use our kernel matrix multiplication method, to calculate the 3x1 repulsive velocity vectors for all the cells (eq. 9).

$$\vec{V}_{rep_{xyz},ijk} = \text{calc\_rep\_vel}(X[i], Y[j], Z[k]) \quad \forall i, j, k \in \{1, 2\} \quad (9)$$

Trilinear interpolation method works on a 3-dimensional regular grid. Before we can start with the interpolation we need to calculate the distance between POI and smaller coordinates of the cells where we calculated the repulsive velocities (eq. 10). The calculated repulsive velocity values are located at the centers of the cells. Therefore, before interpolation, we shift the values of the cells coordinates by half the resolution of the obstacle grid for each direction. That is, the cell coordinates are same as x,y,z, cell index and a half multiplied by grid resolution  $\Delta R$ .

$$\Delta \vec{P} = \begin{bmatrix} \Delta x \\ \Delta y \\ \Delta z \end{bmatrix} = \begin{bmatrix} \frac{(P_x - (X(1) + \frac{1}{2}\Delta R))}{(X(2) - X(1))} \\ \frac{(P_y - (Y(1) + \frac{1}{2}\Delta R))}{(Y(2) - Y(1))} \\ \frac{(P_z - (Z(1) + \frac{1}{2}\Delta R))}{(Z(2) - Z(1))} \end{bmatrix} \quad (10)$$

The result of the interpolation is agnostic of the order of the operations. We first interpolate along the x-axis, followed by along the y-axis and finally along z-axis.

$$\vec{V}_{rep_{xyz},jk} = \vec{V}_{rep_{xyz},0jk}(1 - \Delta x) + \vec{V}_{rep_{xyz},1jk} \Delta x \quad \forall j, k \in \{1, 2\} \quad (11)$$

equations break column

$$\vec{V}_{rep_{xyz},k} = \vec{V}_{rep_{xyz},0k}(1 - \Delta y) + \vec{V}_{rep_{xyz},1k} \Delta y \quad \forall k \in \{1, 2\} \quad (12)$$

$$\vec{V}_{rep_{xyz}} = \vec{V}_{rep_{xyz},0}(1 - \Delta z) + \vec{V}_{rep_{xyz},1} \Delta z \quad (13)$$

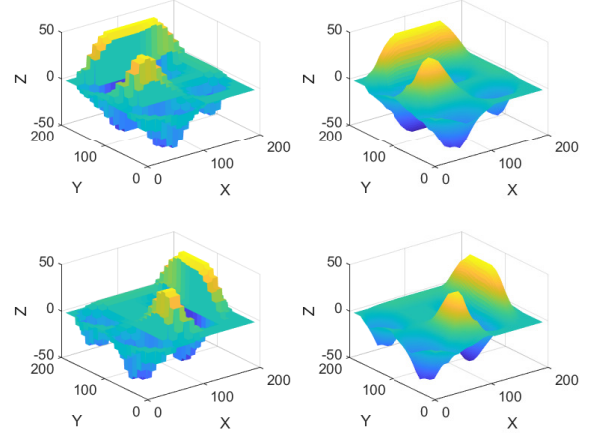


Fig. 1. Repulsive field generation via convolutional kernels. Left: Original repulsive fields in X (top) and Y (bottom) directions. Right: Corresponding fields using interpolation, showcasing enhanced smoothness.

The end product is a uniformly smooth repulsive velocity field, facilitating continuous transitions across discrete points determined within the obstacle grid.

#### IV. MANIPULATOR KINEMATICS

##### A. INVERSE KINEMATIC CONTROL

The desired movement of the end-effector is achieved by using inverse kinematics velocity control scheme with task prioritisation.

$$\dot{\vec{q}} = \mathbf{J}^+ \xi_p \dot{\vec{v}}_{att} + \dot{\vec{q}}_{rep} \quad (14)$$

The damped Moore-Penrose pseudo-inverse,  $\mathbf{J}^+ = \mathbf{J}'(\mathbf{J}\mathbf{J}' + \sigma_{ee}\mathbf{I})^{-1}$ , is utilized to mitigate singularity issues and improve numerical stability in inverse kinematics computations.  $\xi_p$  is the primary task execution slowdown constant. Finally  $\dot{\vec{q}}_{rep}$  are the weighted sum of avoidance joint velocities, each transformed into the null space of primary velocities, as described in the chapter below.

We run the inverse kinematics algorithm once for every time step, until we reach the desired cost function or reach the selected time limit.

##### B. END-EFFECTOR VELOCITY

Prioritizing control over the end-effector's (EE) translational velocity is essential for a consistent and stable target approach. The commonly used method, where translational velocity is proportional to squared distance, leads to impractically high initial velocities, which can prevent obstacle avoidance and real-world execution, followed by disproportionately slow velocities when nearing the goal position. Our aim is a consistent velocity profile throughout the trajectory, with controlled deceleration near the goal. This is achieved by first calculating the unit vector towards the target for direction, then modulating its magnitude using a sigmoid function, specifically the arctangent function (Eq. 15).

$$\vec{v} = \frac{\vec{x}_{EE} - \vec{x}_g}{\|\vec{x}_{EE} - \vec{x}_g\|} \times \frac{\arctan(k_{sigm} \|\vec{x}_{EE} - \vec{x}_g\|)}{\pi/2} \quad (15)$$

In Eq. 15,  $\vec{v}$  specifies the end-effector's (EE) translational velocity directed towards the target, integrating both its direction and magnitude. Here,  $\vec{x}_{EE}$  represents the EE's current position, and  $\vec{x}_g$  is the target position, both in Cartesian coordinates. The calculation  $\frac{\vec{x}_{EE} - \vec{x}_g}{\|\vec{x}_{EE} - \vec{x}_g\|}$  generates a unit vector pointing towards the target, ensuring targeted movement. The velocity's modulation by the arctangent sigmoid function curtails overshooting by moderating speed in proximity to the target and saturating velocity at a predefined upper limit when distant. The parameter  $k_{sigm}$  in the arctangent function adjusts the curve's steepness, affecting how quickly the end-effector decelerates near the target. A higher  $k_{sigm}$  maintains speed until closer to the target for a sharp deceleration, while a lower value starts slowing down earlier for a gradual approach.

The rotational velocity error of the EE is needed for ensuring goal orientation of the EE. In our approach, orientations are depicted using rotation matrices. Specifically,  $R$  represents the current EE orientation, while  $gR$  signifies the goal EE orientation. The disparity between these orientations is encapsulated by the relative rotation matrix  $dR$ . This matrix is formulated by multiplying the goal orientation matrix  $gR$  with the transpose of the current orientation matrix  $cR^T$ . To ensure that it represents a pure rotation without any scaling we then normalize the so gotten matrix .

$$dR = \frac{gR \cdot cR^T}{\|gR \cdot cR^T\|} \quad (16)$$

The relative rotation matrix value is converted into a quaternion, which is then logarithmically transformed ~~to represent the rotational error vectorially~~. The components of this quaternion, excluding the real part, then form the rotational error vector  $\omega$ .

$$dR \mapsto dQ = a + bi + cj + dk \quad (17)$$

$$dQl = 2 \cdot \log(dQ) = al + bl i + cl j + dl k \quad (18)$$

There needs to be an explanation why log, where is this from. Maybe a reference. cite: DMP Quaternions article Petrič, Žlajpah, Ude

$$\vec{\omega} = \begin{bmatrix} bl \\ cl \\ dl \end{bmatrix} \quad (19)$$

To get the full velocity of the end effector (EE),  $\tilde{v}_{ATT}$ , we combine translational and rotational velocities, which we scale using proportional gains  $k_p$  and  $k_r$ .

$$\tilde{v}_{att} = \begin{bmatrix} k_p v * \vec{v} \\ k_r * \vec{\omega} \end{bmatrix} \quad (20)$$

Ker uporabljamo preslikavo v ničelni prostor primarne hitrosti (null space), lahko v primeru velikih hitrosti primarne

naloge preostane premalo prostostnih stopenj, da bi se lahko varno izognili oviram.

To ensure the primary task doesn't overpower the secondary task, we've integrated a primary task execution slowdown. This mechanism can reduce the manipulator's velocity towards its primary goal, leaving more maneuverability space for the secondary tasks.

$$\xi_p = \frac{1}{1 + \kappa_{sec} \delta_{min}} \quad (21)$$

The slowdown factor (eq. 21) is influenced by the constant  $\kappa_{sec}$  and the robot's minimum distance from an obstacle  $\delta_{min}$ . We calculate the minimal distance in the repulsive velocities phase of the algorithm, as explained in section ???. As per the equation, a large  $\delta_{min}$  minimizes the slowdown effect, allowing uninterrupted primary task execution. Conversely, a small  $\delta_{min}$  increases the slowdown, by making the  $\xi_p$  factor smaller, giving the secondary task more time for corrective actions.

### C. AVOIDANCE VELOCITIES

To move the manipulator away from the obstacles in its environment, we cover the manipulator evenly with virtual points. Gostota virtualnih točk je odvisna od velikosti matrik. Če je  $w$  širina matrike v smeri pravokotno na primarno smer, je dobro, če so točke medsebojno razmaknjene glede na potek segmentov za  $\Delta = \frac{w}{3}$ . Tedaj se bodo posamezne matrike deloma pokrivala in dosežemo enakomerno porazdelitev točk (POI) po celotnem robotu. Med izvajanjem kinematične optimizacije izračunavamo izogibne / odbojne hitrosti za vsako od točk po postopku opisanem v zgornjem poglavju. [referenca poglavja](#) To dobimo tako, da izvedemo preslikavo vsake od točk v task space, kjer izvajamo izračun odbojne hitrosti. Pri tem je posamezna kartezična preslikava sestavljena iz kinematične preslikave iz baze robota do začetka segmenta na katerem se točka nahaja in dodane preslikave do izbrane točke (od začetka segmenta do dela kjer se nahaja točka).  $T_{0 \rightarrow POI} = T_{0 \rightarrow 1} \cdot T_{1 \rightarrow 2} \cdot \dots \cdot T_{(j-1) \rightarrow j} \cdot T_{j \rightarrow POI}$  Za vsako od točk dobimo tri komponente kartezične hitrosti.

$$T_{0 \rightarrow POI} = T_{0 \rightarrow 1} \cdot T_{1 \rightarrow 2} \cdot \dots \cdot T_{(j-1) \rightarrow j} \cdot T_{j \rightarrow POI} \quad (22)$$

Ko dobimo za vsako od točk odbojno hitrost (repulsive / avoidance velocity), izračunamo drugo normo vsake od hitrosti. Za  $K$  točk, v katerih so izogibne hitrosti največje in so posledično najbližje oviri nato izračunamo sklepne hitrosti, ki povzročijo izogibanje oviri.

$$J_{d_i}^+ = N J_{d_i}' (J_{d_i}' N J_{d_i}' + \sigma_{rep})^{-1}, \quad \text{for } i = 1, 2, \dots, K; \quad (23)$$

Za vsako od točk na robotu izračunamo Jacobijevo transformacijo hitrosti, ki preslika translacijske hitrosti izbrane točke na robotu iz kartezičnega prostora, v prostor sklepov na robotu, ki povezujejo bazo z izbrano točko. Transformacije kotnih hitrosti v točki nas ne zanimajo. V resnici nas zanima samo komponenta translacijske hitrosti v smeri normale, ki



kaže od najbližje točke na objektu proti izbrani točki interesa (POI) na manipulatorju. Naš prostor operacij se posledično skrči na eno dimenzijo in the Jacobian, which relates the joint space velocities  $\mathbf{q}$  and the velocity in the direction of do, can be calculated as  $J_{d_i} = \tilde{n}_i^T J_i$ . [citat:žlajpah](#) Pri čemer je vektor normale zelene avoidance velocity kar enotski vektor hitrosti, ki ga dobimo s pomočjo naših matrik  $\tilde{n}_i = \frac{\vec{v}_{poi}}{\|\vec{v}_{poi}\|}$ . This method offers computational efficiency by eliminating complex matrix inversions, as the Jacobian changes from matrix into a vector dimensions  $1 \times n$ , where  $n$  is number of joints that are located from before the POI and simplifying repulsive velocity calculations.

$$\dot{q}_{rep} = k_r \sum_{i=1}^K \alpha_i J_{d_i}^+ (v_i - J_{d_i}^+ \xi_p \vec{v}_{att}) \quad (24)$$

Celotne izogibne sklepne hitrosti dobimo z obteženo vsoto izogibnih sklepnih hitrosti izbranih  $K$  najbližjih točk, pri čemer upoštevamo vpliv primarne naloge gibanja vrha manipulatorja na sklepne hitrosti.

## V. SIMULATION RESULTS

### A. Repulsive Field Visualization

We introduce the resultant repulsive field on a two-dimensional map. While analogous principles apply to three-dimensional spaces, visualization of more dimensions is complex. Utilizing our repulsive potential field velocity calculation method, points were sampled across the entire obstacle map as depicted in Figure 2. The prescribed algorithm was executed at each sampled point to derive the repulsive fields along the X and Y axes, which were subsequently visualized as a composite vector field.

### B. Manipulator Examples

#### add the limits of joint positions

The operation of the potential field is demonstrated on two different manipulator cases. The resolution of our voxel grid for obstacles is  $R = 10cm$ . The use of interpolation allows us to have a relatively coarse voxel grid, which reduces the memory demand of the space grid and accelerates the computation. We selected  $K = 7$  Points of Interest (POI) to observe the distance from obstacles and are uniformly distributed them along the segments and joints, starting from the second joint of the robot to the tip of the manipulator. This distribution begins from the second joint because it is from this point onwards that the manipulator has the capability to avoid obstacles. Points of Interest (POIs) are indicated by dots on the manipulator in the graphs. Near obstacles, vectors emanate from these points, depicting the calculated repulsive velocities at the locations. Throughout the simulation, Euler integration of the calculated joint velocities is performed with a step size of  $T_{step} = 0.1$  s.

In the first case (Fig. 3, 4), the manipulator safely 'curls' or selects a path to a point located on the other side of a column, avoiding the obstacle with the potential field calculated by the proposed method. The constants chosen for the primary task are  $k_v = 5$  and  $k_w = 1.5$ , for the avoidance task  $k_r =$

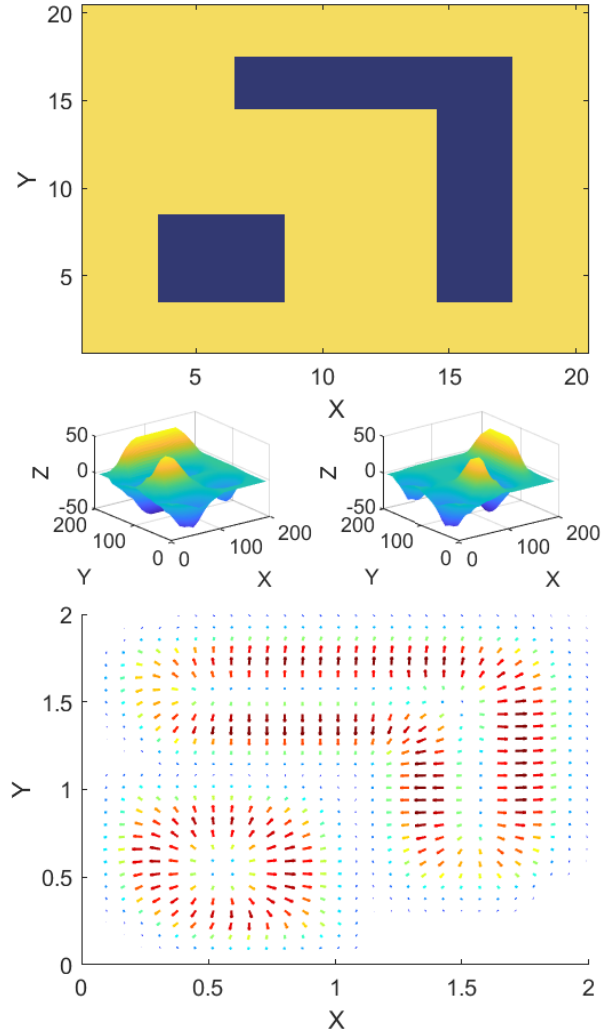


Fig. 2. Visualization of the potential field calculated for the entire map using the proposed approach. Top: Obstacle distribution via a 2D heatmap. Center: Induced repulsive fields along X (left) and Y (right) axes. Bottom: Composite vector field showcasing the resultant repulsive velocities for obstacle avoidance.

20. The weighting constants for the individual POIs are  $\alpha = \frac{[\frac{3}{5}, \frac{2}{5}, \frac{1}{5}, \frac{1}{5}, \frac{1}{5}, \frac{1}{5}, \frac{1}{5}]}{10}$ , where the biggest weight belongs to the point on the manipulator which is closest to the obstacle and so on. As the most direct path for the end-effector to the target passes straight through the column, an approach that would result in a collision, we implement a reduction of the primary speed in the vicinity of the obstacle, setting  $\xi_p = 1$ . The simulation is performed for 50 steps.

In the second scenario (Fig. 5, 6), our robot operates within a dynamic environment. The proposed method for calculating repulsive velocities proves to be a suitable choice when a local optimization approach is needed to accommodate dynamic changes. In this scenario, a ball moves consistently

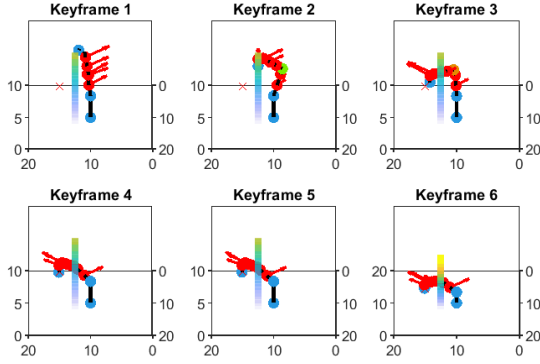


Fig. 3. Sequential keyframes demonstrating the manipulator's path planning and column obstacle avoidance strategy.

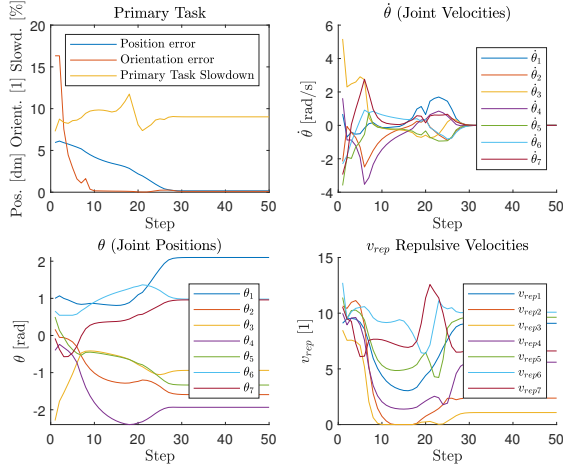


Fig. 4. Visualization of the manipulator's path around the column obstacle: (a) Primary Task errors and percentage of the primary speed after applying slowdown, (b) Joint Velocities  $\dot{\theta}$ , (c) Joint Positions  $\theta$ , and (d) Norms of Repulsive Velocities  $v_{rep}$ .

from the left to the right side of the graph (i.e., along the y-axis from 0.4 at the initial moment to 1.4 in the final step of the simulation), as governed by the equation  $y_{ball} = 0.4 + (1.4 - 0.4) \times \frac{N_{step}}{75}$ , with  $x_{ball} = 1.25$  and  $z_{ball} = 0.7$ . The primary task is now to maintain the robot's end-effector (EE) at a fixed point, disregarding EE orientation to enhance obstacle avoidance capability. This increases maneuverability, thereby eliminating the need for primary speed task slowdown ( $\xi_p = 0$ ). Constants selected for the primary task are  $k_v = 2$  and  $k_w = 0$ , and for the avoidance task  $k_r = 3$ . Weighting constants for the individual POIs are  $\alpha = \frac{[\frac{1}{5}, \frac{1}{5}, \frac{1}{5}, \frac{1}{5}, \frac{1}{5}, \frac{1}{5}, \frac{1}{5}]}{10}$ . The simulation is performed for 75 steps.

describe weights and distributions used in the kernels  
sigmoid weights

## VI. CONCLUSION

TODO

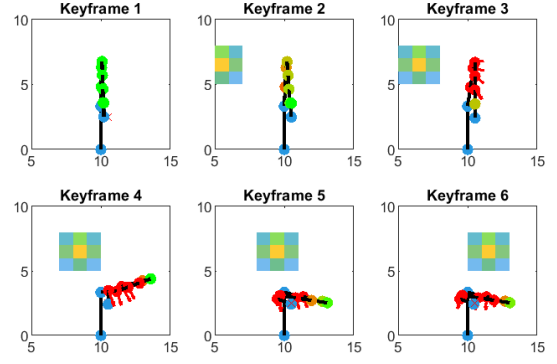


Fig. 5. Dynamic obstacle avoidance scenario: Sequential keyframes illustrating the robot's maneuvering in response to a progressively moving ball from left to right across the workspace.

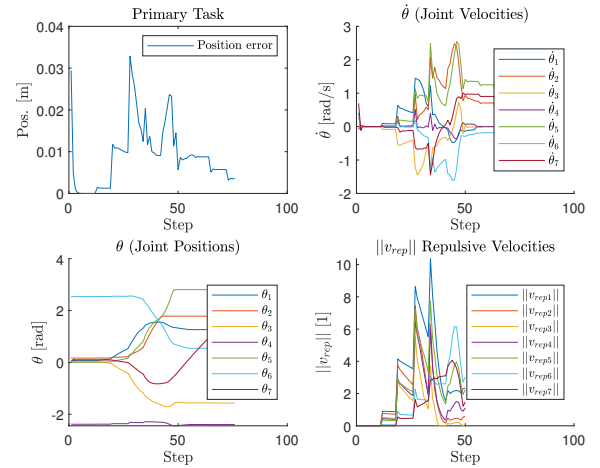


Fig. 6. Performance in a dynamic obstacle avoidance scenario: (a) Primary Task error (b) Joint Velocities  $\dot{\theta}$ , (c) Joint Positions  $\theta$ , and (d) Norms of Repulsive Velocities  $v_{rep}$ .

## REFERENCES

- [1] IDEAS Lab, "Motion and Path Planning," presented at Purdue University, 2023. [Online]. Available: <https://ideas.cs.purdue.edu/research/robotics/planning/>. Accessed on: Jan. 9, 2024.
- [2] E. A. Basso and K. Y. Pettersen, "Task-Priority Control of Redundant Robotic Systems using Control Lyapunov and Control Barrier Function based Quadratic Programs," in IFAC-PapersOnLine, vol. 53, no. 2, pp. 9037–9044, 2020. doi: 10.1016/j.ifacol.2020.12.2024.
- [3] H. Toshani and M. Farrokhi, "Real-time inverse kinematics of redundant manipulators using neural networks and quadratic programming: A Lyapunov-based approach," Robotics and Autonomous Systems, vol. 62, no. 6, pp. 766–781, Jun. 2014. doi: 10.1016/j.robot.2014.02.005.
- [4] J. Haviland and P. Corke, "NEO: A Novel Expeditious Optimisation Algorithm for Reactive Motion Control of Manipulators," IEEE Robot. Autom. Lett., vol. 6, no. 2, Art. no. 2, Apr. 2021, doi: 10.1109/LRA.2021.3056060.
- [5] Y. Zhang, S. S. Ge, and T. H. Lee, "A Unified Quadratic-Programming-Based Dynamical System Approach to Joint Torque Optimization of Physically Constrained Redundant Manipulators," IEEE Trans. Syst., Man, Cybern. B, vol. 34, no. 5, pp. 2126–2132, Oct. 2004. doi: 10.1109/TSMCB.2004.830347.
- [6] J. Nakanishi, R. Cory, M. Mistry, J. Peters, and S. Schaal, "Comparative experiments on task space control with redundancy resolution," in Proc. 2005 IEEE/RSJ Int. Conf. on Intelligent Robots

- and Systems, Edmonton, Alta., Canada, 2005, pp. 3901–3908. doi: 10.1109/IROS.2005.1545203.
- [7] M. H. Raibert and J. J. Craig, “Hybrid Position/Force Control of Manipulators,” *Journal of Dynamic Systems, Measurement, and Control*, vol. 103, no. 2, pp. 126–133, Jun. 1981. doi: 10.1115/1.3139652.
- [8] T. Yoshikawa, “Dynamic hybrid position/force control of robot manipulators—Description of hand constraints and calculation of joint driving force,” *IEEE J. Robot. Automat.*, vol. 3, no. 5, pp. 386–392, Oct. 1987. doi: 10.1109/JRA.1987.1087120.
- [9] O. Khatib, “A unified approach for motion and force control of robot manipulators: The operational space formulation,” *IEEE J. Robot. Automat.*, vol. 3, no. 1, pp. 43–53, Feb. 1987. doi: 10.1109/JRA.1987.1087068.
- [10] N. Hogan, “Impedance Control: An Approach to Manipulation,” in *Proc. 1984 American Control Conf.*, San Diego, CA, USA, Jul. 1984, pp. 304–313. doi: 10.23919/ACC.1984.4788393.
- [11] A. A. Maciejewski and C. A. Klein, “Obstacle Avoidance for Kinetically Redundant Manipulators in Dynamically Varying Environments,” *The International Journal of Robotics Research*, vol. 4, no. 3, pp. 109–117, Sep. 1985. doi: 10.1177/027836498500400308.
- [12] L. Lajpah and T. Petri, “Obstacle Avoidance for Redundant Manipulators as Control Problem,” in *Serial and Parallel Robot Manipulators - Kinematics, Dynamics, Control and Optimization*, S. Kucuk, Ed. InTech, 2012. doi: 10.5772/32651.
- [13] R. Colbaugh and K. Glass, “Cartesian control of redundant robots,” *J. Robotic Syst.*, vol. 6, no. 4, pp. 427–459, Aug. 1989. doi: 10.1002/rob.4620060409.
- [14] K. Glass, R. Colbaugh, D. Lim, and H. Seraji, “Real-time collision avoidance for redundant manipulators,” *IEEE Trans. Robot. Automat.*, vol. 11, no. 3, pp. 448–457, Jun. 1995. doi: 10.1109/70.388789.
- [15] O. Khatib, “Real-time obstacle avoidance for manipulators and mobile robots,” in *1985 IEEE International Conference on Robotics and Automation Proceedings*, Mar. 1985, pp. 500–505. doi: 10.1109/ROBOT.1985.1087247.
- [16] L. Sciavicco and B. Siciliano, “A solution algorithm to the inverse kinematic problem for redundant manipulators,” *IEEE J. Robot. Automat.*, vol. 4, no. 4, pp. 403–410, Aug. 1988. doi: 10.1109/56.804.
- [17] L. Sciavicco and B. Siciliano, “Solving the Inverse Kinematic Problem for Robotic Manipulators,” in *RoManSy 6*, A. Morecki, G. Bianchi, and K. Kedzior, Eds., Boston, MA: Springer US, 1987, pp. 107–114. doi: 10.1007/978-1-4684-6915-8\_9.
- [18] O. Egeland, “Task-space tracking with redundant manipulators,” *IEEE J. Robot. Automat.*, vol. 3, no. 5, pp. 471–475, Oct. 1987. doi: 10.1109/JRA.1987.1087118.
- [19] H. Seraji, “Configuration control of redundant manipulators: theory and implementation,” *IEEE Trans. Robot. Automat.*, vol. 5, no. 4, pp. 472–490, Aug. 1989. doi: 10.1109/70.88062.
- [20] Y. Nakamura, H. Hanafusa, and T. Yoshikawa, “Task-Priority Based Redundancy Control of Robot Manipulators,” *The International Journal of Robotics Research*, vol. 6, no. 2, pp. 3–15, Jun. 1987. doi: 10.1177/027836498700600201.
- [21] B. Siciliano and O. Khatib, Eds., *Springer Handbook of Robotics*. in *Springer Handbooks*. Cham: Springer International Publishing, 2016. doi: 10.1007/978-3-319-32552-1.
- [22] J.-O. Kim and P. Khosla, “Real-Time Obstacle Avoidance Using Harmonic Potential Functions,” 1992. doi: 10.1109/70.143352.
- [23] L. Zlajpah and B. Nemec, “Kinematic control algorithms for on-line obstacle avoidance for redundant manipulators,” in *Proc. IEEE/RSJ International Conference on Intelligent Robots and Systems*, Lausanne, Switzerland, 2002, pp. 1898–1903. doi: 10.1109/IRDS.2002.1044033.
- [24] T. Petrič and L. Žlajpah, “Smooth continuous transition between tasks on a kinematic control level: Obstacle avoidance as a control problem,” *Robotics and Autonomous Systems*, vol. 61, no. 9, Art. no. 9, Sep. 2013. doi: 10.1016/j.robot.2013.04.019.
- [25] M. F. Pinto, T. R. F. Mendonça, L. R. Olivi, E. B. Costa, and A. L. M. Marcato, “Modified approach using variable charges to solve inherent limitations of potential fields method,” in *Proc. 2014 11th IEEE/IAS International Conference on Industry Applications*, Dec. 2014, pp. 1–6. doi: 10.1109/INDUSCON.2014.7059414.
- [26] Z. Long, “Virtual target point-based obstacle-avoidance method for manipulator systems in a cluttered environment,” *Engineering Optimization*, vol. 52, no. 11, Art. no. 11, Nov. 2020. doi: 10.1080/0305215X.2019.1681986.
- [27] A. H. Qureshi and Y. Ayaz, “Potential Functions based Sampling

- Heuristic For Optimal Path Planning,” *Auton Robot*, vol. 40, no. 6, Art. no. 6, Aug. 2016. doi: 10.1007/s10514-015-9518-0.
- [28] A. H. Qureshi et al., “Adaptive Potential guided directional-RRT\*,” in *Proc. 2013 IEEE International Conference on Robotics and Biomimetics (ROBIO)*, Shenzhen, China, Dec. 2013, pp. 1887–1892. doi: 10.1109/ROBIO.2013.6739744.
- [29] J. Yi, Q. Yuan, R. Sun, and H. Bai, “Path planning of a manipulator based on an improved P-RRT\* algorithm,” *Complex Intell. Syst.*, vol. 8, no. 3, pp. 2227–2245, Jun. 2022. doi: 10.1007/s40747-021-00628-y.
- [30] T. Zhu, J. Mao, L. Han, C. Zhang, and J. Yang, “Real-Time Dynamic Obstacle Avoidance for Robot Manipulators Based on Cascaded Nonlinear MPC With Artificial Potential Field,” *IEEE Trans. Ind. Electron.*, pp. 1–11, 2023. doi: 10.1109/TIE.2023.3306405.
- [31] X. Xia et al., “Path Planning for Obstacle Avoidance of Robot Arm Based on Improved Potential Field Method,” *Sensors*, vol. 23, no. 7, Art. no. 7, Apr. 2023. doi: 10.3390/s23073754.
- [32] Y. Chen, L. Chen, J. Ding, and Y. Liu, “Research on Real-Time Obstacle Avoidance Motion Planning of Industrial Robotic Arm Based on Artificial Potential Field Method in Joint Space,” *Applied Sciences*, vol. 13, no. 12, p. 6973, Jan. 2023. doi: 10.3390/app13126973.
- [33] S. M. LaValle, *Planning Algorithms*. Cambridge: Cambridge University Press, 2006.
- [34] M. G. Tamizi, M. Yaghoubi, and H. Najjaran, “A review of recent trend in motion planning of industrial robots,” *Int J Intell Robot Appl*, vol. 7, no. 2, Art. no. 2, Jun. 2023. doi: 10.1007/s41315-023-00274-2.
- [35] P. Švestka and M. H. Overmars, “Motion planning for carlike robots using a probabilistic learning approach,” *The International Journal of Robotics Research*, vol. 16, no. 2, pp. 119–143, 1997.
- [36] S. LaValle, “Rapidly-exploring random trees: A new tool for path planning,” *Research Report 9811*, 1998.
- [37] J. D. Gammell, S. S. Srinivasa, and T. D. Barfoot, “Batch Informed Trees (BIT\*): Sampling-based Optimal Planning via the Heuristically Guided Search of Implicit Random Geometric Graphs,” in *Proc. of the 2015 IEEE International Conference on Robotics and Automation (ICRA)*, May 2015, pp. 3067–3074. doi: 10.1109/ICRA.2015.7139620.
- [38] S. Karaman and E. Frazzoli, “Incremental sampling-based algorithms for optimal motion planning,” in *Proc. Robotics: Science and Systems (RSS)*, 2010.
- [39] J. D. Gammell, S. S. Srinivasa, and T. D. Barfoot, “Informed RRT\*: Optimal sampling-based path planning focused via direct sampling of an admissible ellipsoidal heuristic,” in *Proc. of the 2014 IEEE/RSJ International Conference on Intelligent Robots and Systems*, Chicago, IL, USA, Sep. 2014, pp. 2997–3004. doi: 10.1109/IROS.2014.6942976.
- [40] J. J. Kuffner and S. M. LaValle, “RRT-connect: An efficient approach to single-query path planning,” in *Proceedings of the 2000 ICRA. Millennium Conference. IEEE International Conference on Robotics and Automation. Symposia Proceedings (Cat. No.00CH37065)*, Apr. 2000, pp. 995–1001 vol.2. doi: 10.1109/ROBOT.2000.844730.
- [41] B. Siciliano, “Kinematic control of redundant robot manipulators: A tutorial,” *J. Intell. Robot. Syst.*, vol. 3, no. 3, Art. no. 3, 1990, doi: 10.1007/BF00126069.
- [42] B. Siciliano and O. Khatib, Eds., *Springer Handbook of Robotics*, in *Springer Handbooks*. Cham: Springer International Publishing, 2016. doi: 10.1007/978-3-319-32552-1.
- [43] B. Siciliano, L. Sciavicco, L. Villani, and G. Oriolo, *Robot. Model. Plan. Control*, 2010, pp. 161–189. [Online]. Available: [http://link.springer.com/10.1007/978-1-84628-642-1\\_4](http://link.springer.com/10.1007/978-1-84628-642-1_4)
- [44] Y. Dai, C. Xiang, Y. Zhang, Y. Jiang, W. Qu, and Q. Zhang, “A Review of Spatial Robotic Arm Trajectory Planning,” *Aerospace*, vol. 9, p. 361, Jul. 2022, doi: 10.3390/aerospace9070361.
- [45] S. Gottschalk, M. C. Lin, and D. Manocha, “OBBTree: a hierarchical structure for rapid interference detection,” in *Proceedings of the 23rd Annual Conference on Computer Graphics and Interactive Techniques*, ACM, Aug. 1996, pp. 171–180. doi: 10.1145/237170.237244.
- [46] G. van den Bergen, “Efficient Collision Detection of Complex Deformable Models using AABB Trees,” *Journal of Graphics Tools*, vol. 2, no. 4, pp. 1–13, 1997. doi: 10.1080/10867651.1997.10487480.
- [47] G. Chen, D. Liu, Y. Wang, Q. Jia, and X. Zhang, “Path planning method with obstacle avoidance for manipulators in dynamic environment,” *International Journal of Advanced Robotic Systems*, vol. 15, no. 6, Art. no. 1729881418820223, Nov. 2018, doi: 10.1177/1729881418820223.



- [48] D. Puiu and F. Moldoveanu, "Real-time collision avoidance for redundant manipulators," in Proc. of the 2011 6th IEEE International Symposium on Applied Computational Intelligence and Informatics (SACI), Timisoara, Romania, 2011, pp. 403–408, doi: 10.1109/SACI.2011.5873037.
- [49] H. Oleynikova, Z. Taylor, M. Fehr, R. Siegwart, and J. Nieto, "Voxblox: Incremental 3D Euclidean Signed Distance Fields for on-board MAV planning," in Proc. of the 2017 IEEE/RSJ International Conference on Intelligent Robots and Systems (IROS), Vancouver, BC, Sep. 2017, pp. 1366–1373. doi: 10.1109/IROS.2017.8202315.
- [50] K. M. Wurm, A. Hornung, M. Bennewitz, C. Stachniss, and W. Burgard, "OctoMap: A Probabilistic, Flexible, and Compact 3D Map Representation for Robotic Systems," [Details of publication, e.g., in Proc. of the Conference/Journal Name, Year, pp. Page numbers]. [DOI or URL if available].
- [51] F. Gao, W. Wu, W. Gao, and S. Shen, "Flying on point clouds: Online trajectory generation and autonomous navigation for quadrotors in cluttered environments," *Journal of Field Robotics*, vol. 36, no. 4, pp. 710–733, 2019, doi: 10.1002/rob.21842.
- [52] A. Elfes, "Using occupancy grids for mobile robot perception and navigation," *Computer*, vol. 22, no. 6, pp. 46–57, Jun. 1989, doi: 10.1109/2.30720.
- [53] L. Han, F. Gao, B. Zhou, and S. Shen, "FIESTA: Fast Incremental Euclidean Distance Fields for Online Motion Planning of Aerial Robots," *arXiv*, Jul. 26, 2019. Accessed: Jan. 11, 2024. [Online]. Available: <http://arxiv.org/abs/1903.02144>
- [54] Y. Xu, X. Tong, and U. Stilla, "Voxel-based representation of 3D point clouds: Methods, applications, and its potential use in the construction industry," *Automation in Construction*, vol. 126, p. 103675, Jun. 2021, doi: 10.1016/j.autcon.2021.103675.
- [55] M. Nießner, M. Zollhöfer, S. Izadi, and M. Stamminger, "Real-time 3D reconstruction at scale using voxel hashing," *ACM Trans. Graph.*, vol. 32, no. 6, pp. 1–11, Nov. 2013, doi: 10.1145/2508363.2508374.
- [56] I. Dryanovski, W. Morris, and J. Xiao, "Multi-volume occupancy grids: An efficient probabilistic 3D mapping model for micro aerial vehicles," in Proc. of the 2010 IEEE/RSJ International Conference on Intelligent Robots and Systems, Taipei, Oct. 2010, pp. 1553–1559. doi: 10.1109/IROS.2010.5652494.
- [57] S. Thrun, *Probabilistic robotics*, vol. 45, 2002. Accessed: Jun. 14, 2023. [Online]. Available: <https://dl.acm.org/doi/10.1145/504729.504754>
- [58] B. Lau, C. Sprunk, and W. Burgard, "Improved updating of Euclidean distance maps and Voronoi diagrams," in Proc. of the 2010 IEEE/RSJ International Conference on Intelligent Robots and Systems, Taipei, Oct. 2010, pp. 281–286. doi: 10.1109/IROS.2010.5650794.
- [59] L. Luo et al., "Collision-Free Path-Planning for Six-DOF Serial Harvesting Robot Based on Energy Optimal and Artificial Potential Field," *Complexity*, vol. 2018, pp. 1–12, Nov. 2018, doi: 10.1155/2018/3563846.
- [60] W. Zhang, H. Cheng, L. Hao, X. Li, M. Liu, and X. Gao, "An obstacle avoidance algorithm for robot manipulators based on decision-making force," *Robotics and Computer-Integrated Manufacturing*, vol. 71, p. 102114, Oct. 2021, doi: 10.1016/j.rcim.2020.102114.
- [61] S.-O. Park, M. C. Lee, and J. Kim, "Trajectory Planning with Collision Avoidance for Redundant Robots Using Jacobian and Artificial Potential Field-based Real-time Inverse Kinematics," *Int. J. Control Autom. Syst.*, vol. 18, no. 8, Art. no. 8, Aug. 2020, doi: 10.1007/s12555-019-0076-7.
- [62] D. Han, H. Nie, J. Chen, and M. Chen, "Dynamic obstacle avoidance for manipulators using distance calculation and discrete detection," *Robotics and Computer-Integrated Manufacturing*, vol. 49, pp. 98–104, Feb. 2018, doi: 10.1016/j.rcim.2017.05.013.
- [63] G. Rong and T.-S. Tan, "Jump flooding in GPU with applications to Voronoi diagram and distance transform," in *Proceedings of the 2006 Symposium on Interactive 3D Graphics and Games - SI3D '06*, Redwood City, California, 2006, p. 109. doi: 10.1145/1111411.1111431.
- [64] R. Szeliski, "Computer Vision: Algorithms and Applications, 2nd Edition," Springer, 2021.
- [65] A. Rosenfeld and J. L. Pfaltz, "Distance functions on digital pictures," *Pattern Recognition*, vol. 1, no. 1, pp. 33–61, Jul. 1968, doi: 10.1016/0031-3203(68)90013-7.
- [66] P. F. Felzenszwalb and D. P. Huttenlocher, "Distance Transforms of Sampled Functions," *Theory of Comput.*, vol. 8, no. 1, pp. 415–428, 2012, doi: 10.4086/toc.2012.v008a019.

- [67] X. Zhou, Z. Wang, H. Ye, C. Xu, and F. Gao, "EGO-Planner: An ESDF-Free Gradient-Based Local Planner for Quadrotors," *IEEE Robot. Autom. Lett.*, vol. 6, no. 2, pp. 478–485, Apr. 2021, doi: 10.1109/LRA.2020.3047728.
- [68] I. Dryanovski, W. Morris, and J. Xiao, "Multi-volume occupancy grids: An efficient probabilistic 3D mapping model for micro aerial vehicles," in *2010 IEEE/RSJ International Conference on Intelligent Robots and Systems*, Taipei: IEEE, Oct. 2010, pp. 1553–1559, doi: 10.1109/IROS.2010.5652494.